From Finite Element Simulations to Equivalent Circuit Models of Extracellular Neuronal Recording Systems based on Planar and Mushroom Electrodes

Federico Leva, *Student graduate member, IEEE*, Claudio Verardo, Pierpaolo Palestri, *Senior Member, IEEE*, Luca Selmi, *Fellow, IEEE*

***Abstract*— *Objective:* define a new methodology to build multi-compartment lumped-elements equivalent circuit models for the neuron/electrode systems. *Methods:* the equivalent circuit topology is derived by careful scrutiny of accurate and validated multiphysics finite-elements method (FEM) simulations that couple ion transport in the intra- and extracellular fluids, activation of the neuron membrane ion channels, and signal acquisition by the electronic readout. *Results:* robust and accurate circuit models are systematically derived with the proposed method, suited to represent the dynamics of the sensed extracellular signals over a wide range of geometrical/physical parameters (neuron and electrode sizes, electrolytic cleft thicknesses, readout input impedance, non-uniform ion channel distributions). FEM simulations point out phenomena that escape an accurate description by equivalent circuits; notably: steric effects in the thin electrolytic cleft and the impact of extracellular ion transport on the reversal potentials of the Hodgkin-Huxley neuron model. *Conclusion*: the multi-compartment equivalent circuits derived with our method match with good accuracy the FEM simulations. They unveil the existence of an optimum number of compartments for accurate circuit simulation. FEM simulations suggest that while steric effects are in most instances negligible, the extracellular ion transport remarkably affects the reversal potentials and consequently the recorded signal if the electrolytic cleft becomes thinner than approximately 100 nm. *Significance*: the proposed methodology and circuit models improve upon the existing area and point contact models. The coupling between the extracellular concentrations and reversal potential highlighted by FEM simulations emerges as a challenge for future developments in lumped-element modeling of the neuron/sensor interface.**

***Index Terms*— Modeling and simulation, Extracellular neuronal sensing, Finite-element method (FEM), Lumped-elements equivalent circuits, Micro Electrode Array (MEA)**

I. Introduction

Since many years micro-electrode arrays (MEAs) [1] are the workhorse of *in-vitro* extracellular recording of neuronal electrical activity [2], [3]. Despite their limitations compared to alternative intracellular recording methods [4], they are preferred for their long-term stability [5], CMOS-compatible fabrication process [6], and high parallelism [7], enabling measurements from large neuron populations. MEA design and the interpretation of MEA data require a detailed understanding of the recorded signal generation mechanisms. This task benefits from physics-based distributed models describing the system down to sub-micron scale in combination with reliable equivalent circuit models for the neuron/electrode interaction.

Distributed modeling of extracellular recordings typically relies on the quasistatic approximation of Maxwell equations and on the ohmic assumption for the extracellular fluid [8]. Herein, the resulting system is commonly solved in a *hybrid fashion*: first, the currents of the neuronal membrane are computed according to the cable theory [9] assuming a grounded extracellular domain; second, they are used as sources to compute the extracellular potentials with either analytical approximations [10], [11] or finite-element methods (FEM) [12], [13]. Alternatively, FEM approaches solve *self-consistently* the dynamics of both the intracellular and extracellular fluids with an explicit 3D geometry of the cell membrane [14]–[16]. In all cases, it is possible to include a description of the sensing electrodes [13], [14]. The ohmic assumption can be relaxed by resorting to an electrodiffusive description of the ionic transport phenomena occurring in the cellular fluids. This can be accomplished with hybrid approaches [17] as well as self-consistent formalisms with explicit descriptions of the neural geometries [18], [19]. Electrodiffusive models allow a close inspection of the contribution of each ionic species to the recorded signal and, furthermore, they provide more accurate solutions for spatial resolutions lower than the micrometer [20], a scale which is typical of the neuron/electrode cleft [21]. Notwithstanding, relatively little effort has been made in the past to model the neuron/electrode interaction at the electrodiffusive level [22]. We have recently proposed a novel FEM framework [23], which sets the basis for the present work.

Equivalent circuit models are a widely used alternative to distributed models [24], [25]. Indeed, the cable theory formalism mentioned above [9] is amenable for integrations in circuit simulators [26]–[28]. Building upon this fact, lumped-elements equivalent circuits allowed many groups [29]–[32] to gain insight into how the biological/physical/geometrical parameters of the recording system affect the experimentally recorded signals. Most circuits rely on the *point contact model* [21]: the electrode and the junctional portion of the neuron membrane (i.e., that interfaced to the electrode) are lumped together into a netlist node, under the assumption that the interface is far away from the ground. The electrode is commonly described by passive elements whereas the membrane is represented with different levels of accuracy and complexity (in decreasing order): i) Hodgkin-Huxley (HH) [33] and HH-like models [29] [34], [35] [32], [36], [37]; ii) RC passive driven by voltage/current sources with HH-like waveforms [4], [5], [38]; iii) RC passive with AC input drive [5], [31], [39]. Still, the non-junctional membrane (i.e., that not facing the electrode) can be described by one or more compartments [30], [40]. Ref. [37] demonstrated that the aggregation of HH blocks in a multi-compartmental description of the neuron, in combination with a mono-compartmental circuit description of the junctional neuron/electrode interface, accurately reproduces the waveforms of recorded signals.

However, the point contact model cannot account for distributed effects at the electrode/neuron junction which can modify the local extracellular potential. To this aim, *area contact models* have been

Manuscript received xx xx xx. Date of publication xx xx xx; date of current version xx xx xx. This work has been financially supported by the European Union's Horizon-2020 project "IN-FET" (Grant Agreement n. 862882) via the IUNET consortium.

Federico Leva and Luca Selmi are with the Department of Engineering "Enzo Ferrari", Università degli Studi di Modena e Reggio Emilia, 41125 Modena, Italy (Corresponding author e-mail: luca.selmi@unimore.it).

Claudio Verardo is with The BioRobotics Institute and Department of Excellence in Robotics and AI, Scuola Superiore Sant'Anna, 56127 Pisa, Italy.

Pierpaolo Palestri is with the Polytechnique Department of Engineering and Architecture, Università degli Studi di Udine, 33100 Udine, Italy.

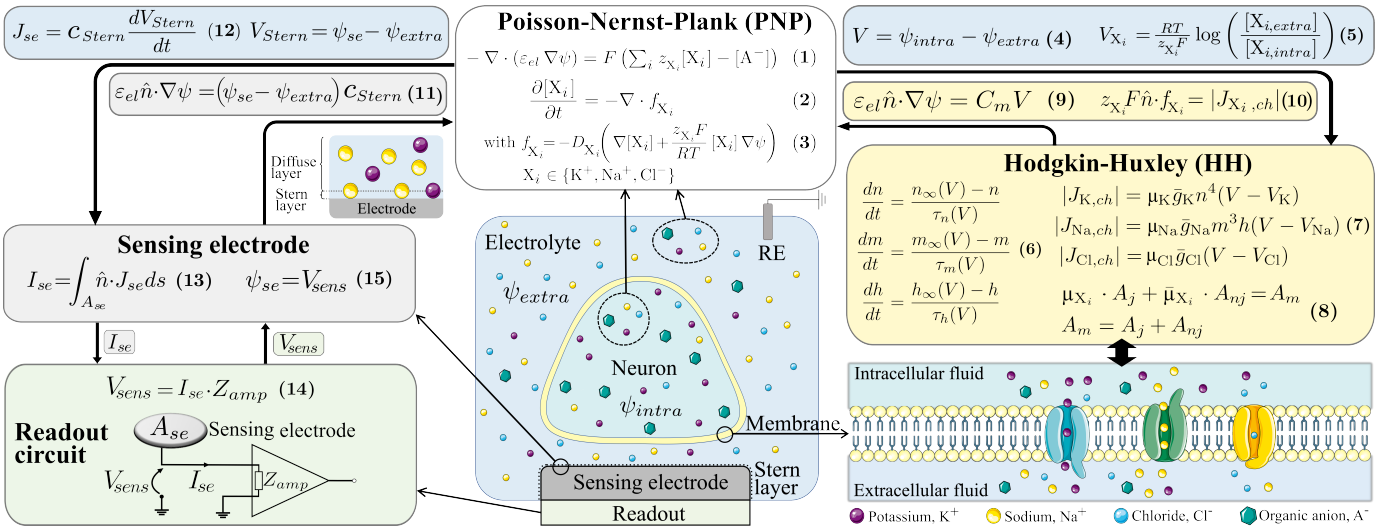

Physical variables: ψ=electrolyte electric potential, $[\mathrm{X}_i]$=concentration of mobile ion i, $[\mathrm{A}^-]$=concentration of fixed anions, f_{X_i}=ion flux, n, m, h=gating variables, $J_{\mathrm{X}_i,ch}$=ion channel current density, μ_{X_i}=channel aggregation factor, V_{X_i}=reversal potential, V=membrane potential, V_{Stern}=potential across the Stern layer, J_{se}=electron current density at the electrode, I_{se}=sensing electrode current toward the readout ($\hat{n}$ is the direction normal to a surface), V_{sens}=readout input voltage, ψ_{se}=electric potential at the electrode. **Physical parameters:** ε_{el}=electrolyte electric permittivity, D_{X_i}=diffusivity of ion i, z_{X_i}=ionic valence, $n_\infty, m_\infty, h_\infty$=(in)activation curves of gating variables, τ_n, τ_m, τ_h=time constants of gating variables, $\bar{g}_{\mathrm{X}_i}$=maximum ion channel conductance per unit area, C_m=membrane capacitance per unit area, c_{Stern}=Stern layer capacitance per unit area, T=temperature, F=Faraday constant, R=gas constant, Z_{amp}=readout input impedance. **Geometrical parameters:** A_{se}=electrode surface area, A_j=junctional membrane area, A_{nj}=non-junctional membrane area, A_m=$A_j + A_{nj}$=total membrane area. (Part of the image is adapted from Servier Medical Art, © CC BY 3.0)

Fig. 1. Sketch of the modeling framework: neuron membrane, intracellular ("neuron") and extracellular ("electrolyte") fluids, sensing electrode, and readout circuitry. The boxes represent different physics, mutually coupled by the equations on the connecting arrows. All the physical variables are space (r, z in a cylindrical reference system) and time (t) dependent (not shown for improved clarity of the equations). The default values of the parameters and variables are given in Table TS1 and TS2 of the Supplementary Information.

proposed [21] that consider more than one compartment for the junction. These models typically describe membranes as distributed RC nets with intracellular potentials/currents left as external sources, e.g., for frequency analysis [41], or describe only the recording device in a distributed fashion while including a single HH compartment for the membrane [42]. To the best of our knowledge, truly distributed *area contact models* with HH-based junction implementation for transient studies are still missing. Ideally, such an equivalent circuit should account for the distributed nature of the neuron/electrode junction *and* of the HH-type membrane, and should adopt a suitable number of compartments to preserve the accuracy of the recorded signal. Physics-based FEM modeling can be used as a testbed to evaluate the accuracy of the circuit across various neuron/electrode/junction geometries and physical parameters, thus reducing the need for experimental data. Such methodology may additionally shed light on i) the minimum number of junctional and non-junctional compartments required; ii) the optimal approach to translate the physical domain into compartments. This work aims to overcome the limitations of most existing area contact models and provide a tool to bridge the gap between these points.

Firstly, we present an extended version of the FEM model proposed in [23] to investigate continuous and non-uniform ion channel distributions, neuron membranes with domed and ellipsoidal shapes, and realistic planar and mushroom geometries of the sensing electrode. Secondly, we propose a method to derive accurate multi-compartmental equivalent circuits for the geometries analyzed with FEM simulations. The circuit and FEM models are compared against simulation and experimental data to prove their accuracy, and then compared to each other to assess the minimum number of compartments necessary to an accurate equivalent circuit model. Finally, we investigate thin junctional clefts, where neglecting the electrodiffusive nature of the extracellular fluid fundamentally degrades the accuracy of the circuit model.

The manuscript proceeds as follows. The FEM simulation framework and the derivation of the equivalent circuit are described and validated in section II. A comparison between the two models and a systematic analysis of how the system geometry and physical properties affect the results are reported in section III. Results are discussed in section IV. Conclusions are finally drawn in section V.

II. Methodology

A. FEM modeling framework

The FEM model is an extension of the one in [23]. It is based on COMSOL Multiphysics® [43] and aims to describe the intra- and extracellular fluids, the neuron membrane, and the metallic electrode coupled to a readout circuit. This is showcased in Figure 1 which also defines the model equations. All physical variables in Figure 1 are space (r and z in a cylindrical reference system) and time (t) dependent, although not explicitly shown. For the sake of a self-contained paper. here we summarize the main model ingredients and the extensions.

Intra- and extracellular fluids are described via the electrodiffusive *Poisson-Nernst-Plank* (PNP) transport model (see (1-3) in Figure 1) [44], implemented via a multiphysics coupling between the "electrostatics" and "transport of diluted species" interfaces from the AC/DC and electrochemistry modules [43]. A reference electrode (RE in Figure 1) is placed to set the ground potential reference in the bulk of the extracellular fluid, where also the ion concentrations are at their baseline value.

The phospholipidic neuron membrane is described with a thin layer approximation according to (9) that saves a fine mesh. This enforces the continuity of the normal component of the displacement field vector across the intra- and extracellular boundaries and naturally creates diffuse layers at these interfaces. Ion channels, fundamental for generating action potentials (APs), are located at each mesh point of the lipidic layer. Their dynamics for AP genesis is described via

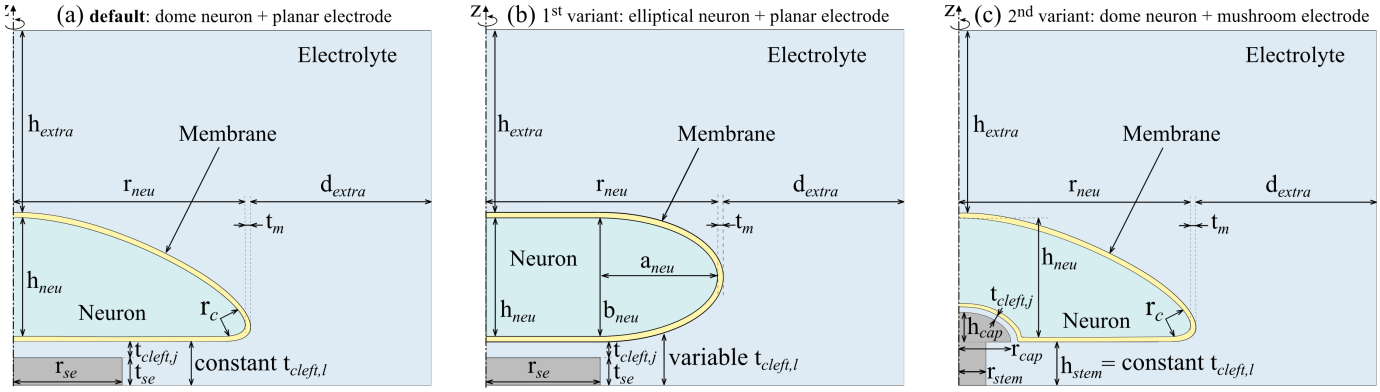

Fig. 2. 2D-cross section (not to scale) of (a and c) a 3D dome and (b) elliptical neurons with cylindrical symmetry around the z-axis. The neurons are in the proximity of (a and b) planar or (c) mushroom-shaped sensing electrodes. The main physical and geometrical parameters are reported in Tables TS1 and TS2 of the Supplementary, respectively. The simulation setup in (a) is used as the *default case* in the following. In the models, the electrode is connected by default to an ideal amplifier's input impedance Z_{amp}=R_{amp}=100 GΩ.

the Hodgkin-Huxley (HH) model [9], [33] assuming a rest membrane potential V_r=-65 mV. The HH's gating variables are computed by solving a set of ordinary differential equations (ODE) at each membrane's mesh point (6). Consequently, the corresponding current density of the ion channels is updated through (7) and applied as boundary flux to the electrolyte according to (10). The transmembrane stimulus to elicit action potentials is an additional Na^+ boundary flux across the upper portion of the neuron membrane (i.e., the one that does not face the electrode and the substrate), which is a simplified model for excitatory synapses [45]. The membrane potential, V in (4), controls the non-linear conductances.

The reversal potentials for the ions are commonly included as constant parameters (i.e., set to their baseline values) in the ODEs. In our case instead, they can be dynamically updated by sampling the ion concentrations at each time step and assuming that changes in the concentrations instantaneously turn into changes in potential through (5). This last option entails that we self-consistently account for the impact of extracellular concentrations on the membrane potential. This topic is examined in subsection III-C.

In addition to our previous work [23], here we also account for uneven distributions of ion channels over the membrane. Indeed, different morphological regions of the same neuron (e.g., soma, dendrites, axon hillock, etc.) have intrinsically different channel densities [46]–[48] which might change locally if a neuron/electrode junction is present [36]. As a support to this claim, fitting of extracellular recordings suggested accumulation/depletion of ion channels (e.g., K^+, Na^+) in rat hippocampal [49], cortical [30] and dorsal root [50] neurons, HEK293 cells [51], human myocardial cells [52]. Furthermore, ion channels can drift-diffuse across the cell membrane [47] and different shapes of extracellular recorded signals are also observed across excitable cells without arborizations, such as chromaffin cells [53]. To reproduce these putative uneven distributions of channels, we alter the maximum channel conductance $\overline{g}_{X_i}$ of ion species X_i in (7) by multiplication for the scalar μ_{X_i}, similarly to [50]. These parameters account for the accumulation (i.e., $\mu_{X_i}>1$) or depletion (i.e., $\mu_{X_i}<1$) of ionic channels at the membrane/electrode interface and the concurrent depletion (i.e., $\overline{\mu}_{X_i}<1$) or accumulation (i.e., $\overline{\mu}_{X_i}>1$) elsewhere in the membrane to maintain constant the overall number of ion channels (see (8)).

The Stern layer on top of the electrode, included via a thin layer approximation, leads to the formation of a diffuse layer in the electrolyte (11) and to a displacement current density entering the electrode (12). No *red-ox* reactions are implemented at the electrode surface. For the sake of computationally efficient calculations and differently from [23], we avoid meshing the bulk of the sensing electrode. Instead, we collect the displacement current signal at the electrode surface (i.e., the integral over the electrode surface area of the displacement current density across the Stern layer, see (13) in Figure 1), that, once entering the input impedance of the underneath readout yields the sensed potential V_{sens} according to (14). The sensed potential itself becomes a boundary condition for the electrostatic potential in the PNP description of the extracellular fluid (15). This creates a bidirectional coupling between the solution of the PNP and that of the sensing electrode. The readout here is simplified with the input impedance of an ideal amplifier, although our approach can in principle include readout circuits of any complexity.

Figure 2 shows the structures considered in the FEM analysis, all featuring cylindrical symmetry. Physical properties and dimensions are respectively reported in Table TS1 and TS2 of the Supplementary.

B. Methodology to derive a lumped-elements equivalent circuit

The lumped-elements equivalent circuit model is based on a few approximations: 1) the electrolyte's reactance is assumed large compared to its parallel resistance, given the time scale of the action potentials; 2) intracellular compartments are assumed equipotential; 3) the electrodes are ideally polarizable; 4) we consider only axis-symmetric structures (i.e., the circular electrode is perfectly aligned with the neuron and are described in a cylindrical reference system).

Figure 3 illustrates the methodology to derive and combine the elementary blocks of the lumped-elements equivalent circuit. The procedure is described here for the dome neuron coupled to the planar electrode of Figure 2.a. It can be adapted to the cases in Figure 2.b and 2.c with minor adjustments addressed in section III.

The *first* step is to partition the *junctional* portion of the neuron membrane (i.e., the one facing the electrode). This is represented by a ring with a small innermost radius of 1 nm (a reasonable approximation for the innermost radius if $r_{ex,1} \gg 1$ nm), and an outermost radius r_{se}. We partition this ring in concentric rings of equal *pitch*:

$$pitch_j = (r_{se} - 1\,\mathrm{nm})/M\,,$$

where M is the number of compartments for the junctional region. The use of rings of equal pitch is the one giving the best agreement between the FEM and the equivalent circuit, although we also considered rings with equal area, still achieving a good mutual agreement (not shown). For each of the M rings, we identify the internal, $r_{in,k}$, and external, $r_{ex,k}$, radii. The area of the *k-th* ring is

$$A_{HH_{j,k}} = \pi(r_{ex,k}^2 - r_{in,k}^2) \qquad (14)$$

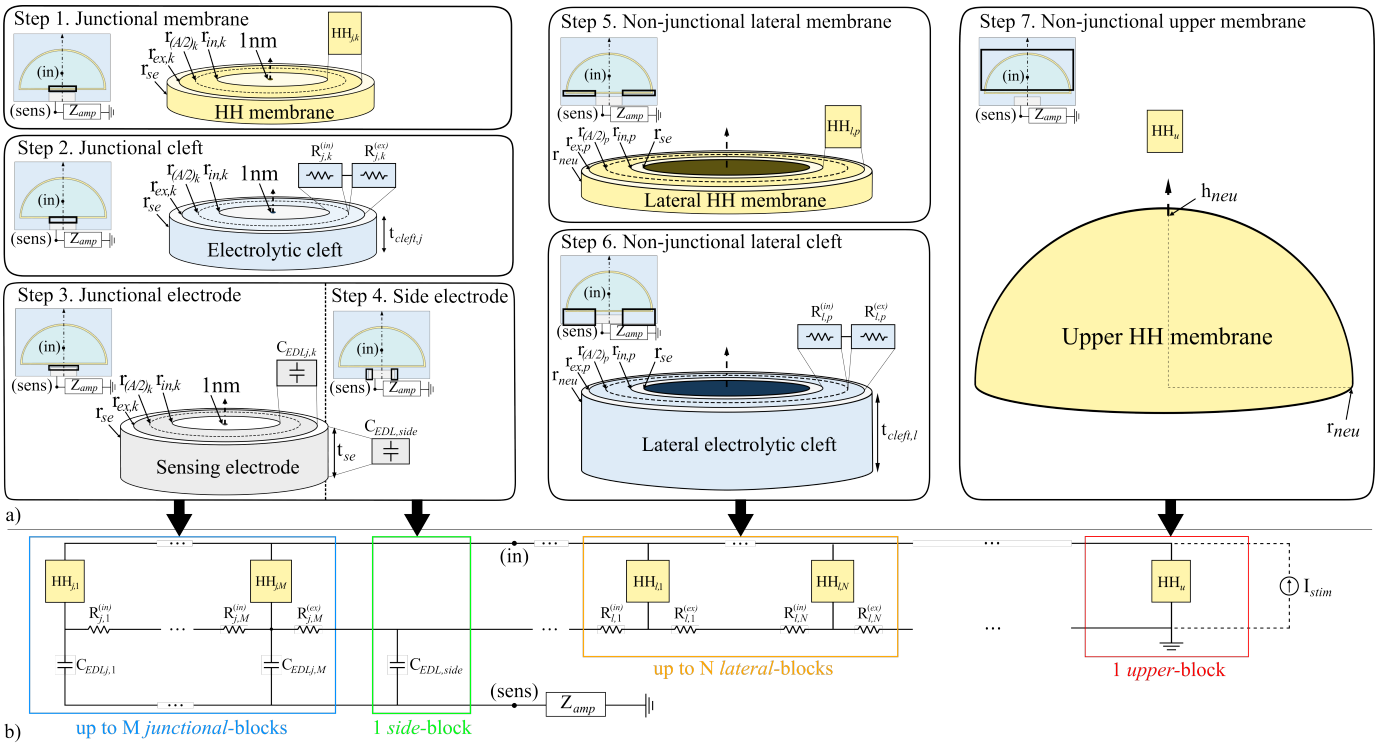

Fig. 3. (a) Flowchart of the algorithm to derive the (b) elementary blocks of the lumped-elements equivalent circuit considering the dome-shaped neuron above to the planar sensing electrode in Figure 2.a. The circuit should be composed of at least one *junctional (j)*, one *side*, and one *upper (u)* block. The *junctional* and *lateral (l)* blocks can be instantiated M and N times, respectively, depending on the desired partitioning degree of the system. It can be adapted to the cases in Figure 2.b and 2.c with minor adjustments that will be addressed in section III.

with $k = \{1, ..., M\}$, $r_{in,1}$=1 nm, and $r_{ex,M}$=r_{se} and is associated with an HH circuit compartment.

Neglecting the polarization effects of the protein-glycocalyx layer in the neuron/electrode cleft [54], each membrane compartment is in direct contact with the underlying portion of the electrolyte cleft (see step 2). In this latter case, careful observation of the FEM simulations shows the presence of a diffuse layer (DL) at the membrane's interface (i.e., ions pile up onto the membrane surface and their concentration decays according to the Debye-length [44]). One might thus expect a DL capacitance, C_{DL}, in between the HH circuit block and the sealing resistances representing the cleft. However, during neuron activity, the ion channels originate a mass transport path through the DL that effectively shortens the C_{DL} at low frequencies, and translates into a DL resistance (R_{DL}) in parallel to C_{DL}. We quantified R_{DL} by means of a few transient simulations (not shown) applying transmembrane ionic current steps, and we confirmed an R_{DL}<1 nΩ·m^2 which short-circuits the DL reactance (≈184 μΩ·m^2 at 1 kHz). As shown in Figure 5.c, an equivalent circuit without R_{DL} generates signals not consistent with the physics-based FEM results. For this reason, in the following we always assume that R_{DL} dominates the conduction and short circuits C_{DL}. Thus, we neglect the C_{DL} at the membrane from the equivalent circuit. We point out that further polarization effects may stem from Stern layers at the neuron membrane, but there is no consensus on the necessity to account for them [32], [37] or not [38] in equivalent circuits. Moreover, there are no available strategies to implement them in FEM models while maintaining the ion concentrations close to the membrane within physiological ranges [23]. Thus, we neglect them, in line with [14].

The *second* step (step 2 in Figure 3) consists in evaluating the sealing resistance of the thin *junctional* electrolytic cleft between the electrode and the membrane of each of the M compartments. Here we assume a radial current density propagation; consistently, for each compartment, we split the cleft's sealing resistance into two concentric contributions, each representing half of the in-plane *area* of the compartment. The first resistance, referred as *internal*, extends from $r_{in,k}$ to the radius $r_{(A/2)_k} = \sqrt{(r_{in,k}^2 + r_{ex,k}^2)/2}$ that divides into two equal parts the *k-th* ring's area and reads:

$$R_{j,k}^{(in)} = \frac{1}{2\pi\sigma_{el} t_{cleft,j}} \ln\left(\frac{r_{(A/2)_k}}{r_{in,k}}\right). \quad (15)$$

The second resistive contribution, referred as *external*, goes from $r_{(A/2)_k}$ to the end of the *k-th* ring, $r_{ex,k}$, and is given by:

$$R_{j,k}^{(ex)} = \frac{1}{2\pi\sigma_{el} t_{cleft,j}} \ln\left(\frac{r_{ex,k}}{r_{(A/2)_k}}\right) \quad (16)$$

where σ_{el} =1.43 S/m [37] is the electrolyte conductivity, $k = \{1, ..., M\}$, $r_{in,1}$=1 nm, and $r_{ex,M}$=r_{se} (consistently with (14)). We verified (not shown) that assigning $R_{j,k}^{(in)}$ and $R_{j,k}^{(ex)}$ according to (15) and (16) rather than splitting the ring resistance into two parts at $(r_{in,k} + r_{ex,k})/2$ leads to a much better agreement between the FEM model and the equivalent circuit.

The choice of (15) and (16), and the considerations on the membrane made above, suggest to connect the terminal of the *k-th* HH compartment to the middle node of the underlying resistive net representing the *k-th* electrolytic cleft. This leads us to build the circuit in Figure 3.b by adding consecutive RC blocks with *"T"*-like topology. Notice that, only for the first block, the $R_{j,1}^{(in)}$ is missing since it does not carry any current (for symmetry reasons).

The *third* and *fourth* steps in Figure 3 account for the *junctional* and *side* portions of the electrode, respectively. By assuming an ideally polarizable metallic electrode (hence, inert in physiological fluid) [23], an electrical double-layer (Stern plus diffuse layers) builds up at the electrolyte-electrode interface, although more complex

circuit models of the electrode surface can be found [55]. This is modeled as an EDL capacitance per unit area, c_{EDL}, computed as the series of c_{Stern} and c_{DL}, multiplied by the junctional electrode surface area of each *k-th* compartment in (14). The EDL capacitance is placed in between the resistances representing the electrolytic cleft, exactly below the corresponding HH compartment. The only exception is for the electrode sidewall (step 4 in Figure 3.a) where

$$C_{EDL,side} = c_{EDL} \cdot (2\pi r_{se} t_{se}) \,, \tag{17}$$

is connected to the sealing resistance representing the most peripheric part of the electrolytic cleft above the electrode. Notice that, differently from the C_{DL} of the membrane, the electrode EDL capacitance should be retained, since there is no redox process nor mass transfer between electrode and fluid.

Step *five* in Figure 3 computes the area of *non-junctional lateral* membrane compartments (i.e., the ones just beside the junctional ones). Similarly to step 1, we partition this lateral ring in N concentric rings of equal *pitch*:

$$pitch_l = (r_{neu} - r_{se})/N \,,$$

where N is the number of the desired compartments for the lateral region. Thus, identifying N internal, $r_{in,p}$, and N external, $r_{ex,p}$, radii, we compute the *p-th* HH compartment's area as:

$$A_{HH_{l,p}} = \pi(r_{ex,p}^2 - r_{in,p}^2) \,, \tag{18}$$

with $p = \{1, ..., N\}$, $r_{in,1}$=r_{se}, and $r_{ex,N}$=r_{neu}.

The *sixth* step determines the value of the internal and external portions of the sealing resistances that describe the electrolytic cleft of the *lateral non-junctional* portion of the neuron, following the same procedure as in step two (see (15-16)). The only difference is that the cleft outside the electrode is thicker than the one above the electrode by a thickness t_{se} (i.e., $t_{cleft,l}$=$t_{cleft,j}$+t_{se}):

$$\begin{aligned} R_{l,p}^{(in)} &= \frac{1}{2\pi\sigma_{el} t_{cleft,l}} \ln\left(\frac{r_{(A/2)_p}}{r_{in,p}}\right) \\ R_{l,p}^{(ex)} &= \frac{1}{2\pi\sigma_{el} t_{cleft,l}} \ln\left(\frac{r_{ex,p}}{r_{(A/2)_p}}\right) . \end{aligned} \tag{19}$$

At the last step, we represent the *upper* part of the neuron membrane (i.e., the one not facing the electrode or the planar substrate) as a unique compartment with half the surface area of an ellipsoid with semi-axis r_{neu} and h_{neu}, as reported in Figure 2.a, and neglecting r_c for simplicity. Since this portion of the membrane faces the bulk electrolyte region connected to the reference electrode, the corresponding HH circuit is connected directly to the ground.

C. Comparison with experimental and simulation data

In this section we compare the FEM and the lumped-element equivalent circuit models against experiments in [56], [57] and simulations in [29], [50] for the purpose of a robust validation of our approach and to show that framework is able to handle many realistic situations. The latter references [29], [50] report all the parameters used in the simulations (see last section of the Suppplementary Information). Moreover, they describe the neuron morphology and processes with a single somatic compartment as done in this work. Therefore, they are ideal sources of information for a reliable test of the newly proposed modeling procedure. This comparison is reported in Figure 4.a and Figure 4.b.

The limited information available on the experiments in [56], [57], instead, forced us to make some assumptions. In particular, we approximate the complex morphology of the cortical neurons in [56], [57] with the single-compartment model for the dynamics of

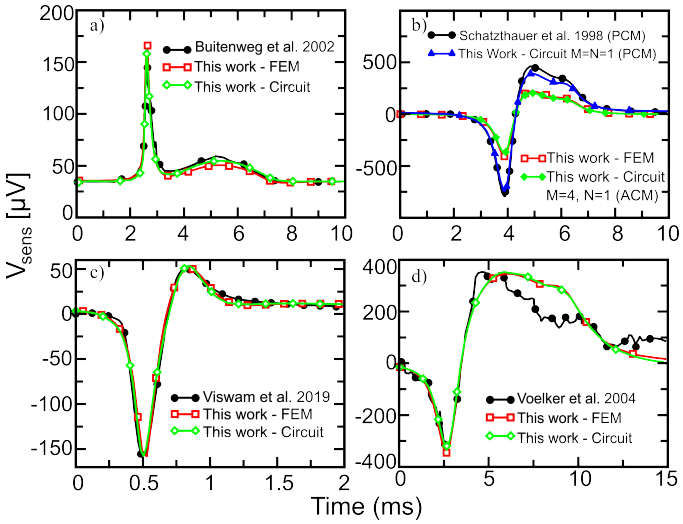

Fig. 4. Comparison of the models of this work with published simulations from [50] (plot a), [29] (plot b), and experimental data from [56] (plot c), and [57] (plot d). For each plot, some simulation model parameters have been adjusted with respect to the default ones (see Supplementary Information) so as to match those of the references.

cortical neurons reported in [58] (with only minor adjustments, see Supplementary Information). Moreover, we assume that the alteration of the ion channels, which in real neurons is distributed over all constituent parts of the cell, can be applied to the unique (effective) somatic compartment of our model [29], [50]. Figure 4.c and d show that in spite of these approximations, our models nicely replicate the traces in Fig. 4.B2 of [56] and in Fig. 3.B of [57] by adjusting the thickness of the electrolyte cleft between the neuron and the sensing electrode.

Figure 4 proves that our models are consistent with the literature, and that they can be adapted to replicate experimental traces and, furthermore, supports its use for further analysis.

The comparison of the FEM simulations and area contact model (ACM) circuits (i.e., M=4) to the point contact model (PCM) circuit simulations in Figure 4.b shows that the former capture the effects related to signal averaging due to the distributed nature of the electrode/cleft junction. For the same set of parameters, PCM circuit models (consistent with our approach if M=1) match quite well the waveform shape but predict larger signal amplitudes.

D. Simplification of the equivalent circuit model

In this section, the responses of the equivalent circuit to action potentials (APs) are compared to FEM simulations of the structure in Figure 2.a with default parameters as in Tables TS1 and TS2 of the Supplementary Information. The choice of the parameters for the Hodgkin-Huxley action potential model dynamics is consistent with state-of-the-art circuit models [37], whereas the geometrical set of parameter values (see Table TS2) is consistent with [50].

The APs are elicited by a transmembrane current pulse lasting 0.5 ms and with an amplitude of ≈0.22 nA applied to the *upper* HH compartment (current density of 0.5 A/m^2 in the FEM case). This choice avoids any overlap between the stimulus and the recorded extracellular signal [23], [37], [59]. We account for the accumulation/depletion of channels in the junctional area (and the consequent depletion/accumulation of non-junctional channels) acting on the μ_{X_i} parameter for the sodium and potassium ions in (7) of Figure 1. We sweep one parameter at a time w.r.t. the uniform channel distribution case (i.e., all μ_{X_i}=1). In this latter case, we observe a very small

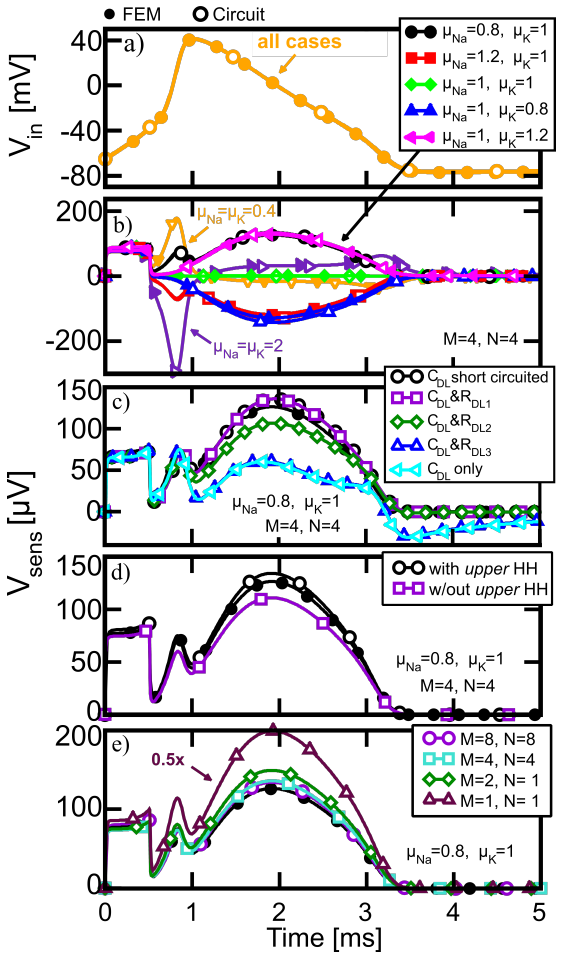

Fig. 5. Intracellular action potential (V_{in}) calculated with the FEM (filled symbols) and circuit (open symbols) models for: (a) and corresponding sensed voltage (V_{sens}) (b-e) due to a transmembrane current stimulus for the default FEM model in Figure 2.a (filled symbols) and the corresponding equivalent circuit model (open symbols) built following the flowchart in Figure 3. (b) Signals sensed by the electrode for different μ_{X_i}. Good agreement between FEM and equivalent circuit is found with M=4, N=4, corresponding to 9 compartments in total. (c) Sensed signals for μ_{Na}=0.8, μ_K=1 for different values of R_{DL} (R_{DL1}=1 nΩ·m^2 (squares), R_{DL2}=10 Ω·m^2 (diamonds), R_{DL3}=1 kΩ·m^2 (triangles up)) placed in parallel to the double layer capacitance C_{DL} (i.e., the capacitance between the HH compartment and the sealing resistances of Figure 3). (d) Sensed signals for M=4, N=4, and μ_{Na}=0.8, μ_K=1 with and without the *upper* HH compartment. (e) V_{sens} computed for μ_{Na}=0.8, μ_K=1 and reducing the number of compartments from 17 (M=8, N=8) to 3 (M=1, N=1). In the last case, the circuit response strongly deviates from the FEM reference.

sensed extracellular signal in the order of nanovolts, in agreement with experiments in [29], [48] and simulations in [36], [50]. This is because the capacitive and ionic currents essentially balance each other; thus, the fA-ranged net current that exits from adjacent HH compartments and flows through the cleft (whose total resistance is in the order of MΩ) cannot produce appreciable extracellular potential variations.

Figure 5 reports the intracellular (plot a) and the sensed (plots b-e) signals for the *default* FEM model in Figure 2.a (filled symbols) and for the equivalent circuit model (open symbols). The intracellular signals in Figure 5.a reproduce the typical AP waveform, and clearly show good agreement between the two modeling approaches. Notice that in the implemented HH model we have kept the parameters for the dynamics of the gating variables at 6.3 °C as obtained in the original HH model [60]. This choice is consistent with other literature works [29], [37]. The use of room temperature for the model parameters would result in slightly shorter AP pulses (not shown, see [61]) and would not affect the results. The AP waveform is the same for most of the case studies examined in this manuscript because any local alteration of the channel density in the junctional part of the membrane (next to the electrode) is compensated by an opposite alteration in the non-junctional part. Therefore, it is not reported again in the following, except for the results in subsection III-C.

Figure 5.b demonstrates that the circuit built following the steps in Figure 3 with M=4, N=4 matches very well the responses of the FEM model for all values of μ_{X_i}. The impact of the choice of M and N will be analyzed at the end of this section. All curves start with a pulse due to the transmembrane current stimulus. The pulse vanishes just before the onset of the extracellular signal activity at 0.5 ms.

Different waveforms can be observed, and interpreted as follows: i) a depletion (black curves)/aggregation (red curves) of only the sodium channels at the sensing electrode makes the Na^+ current smaller/larger than the capacitive current in the fast rising phase of the AP. This non-negligible net current flows through the cleft and generates a voltage drop in the electrolyte surrounding the electrode. As a result, small positive/negative peaks can be observed around 0.8-0.9 ms, respectively. ii) The depletion (blue curves)/aggregation (fuchsia curves) of the potassium channels or a complementary alteration (accumulation (red curves)/depletion (black curves)) of sodium channels at the sensing electrode has similar effects on the slow-falling phase of the AP, as visible by the negative/positive peaks at about 2 ms. This is consistent with the complementary roles of the Na^+ and K^+ channels. iii) As expected, almost zero (few nVs) voltage signals are attained if the channel distribution is uniform (green curves). Waveforms i-iii) are consistent with those reported in [50]. iv) If the Na^+ and K^+ channels are simultaneously unbalanced in the same direction (μ_K=μ_{Na}=0.4 and 2, orange and violet curves), the early peak at 0.8 ms is further enhanced. These are two relevant conditions that resemble the typical biphasic shape of the positive/negative derivative of the intracellular AP as reported in simulation/experimental data [29], consistent with Figure 4.b. Also in this case, as in i-iii, the response of the circuit matches well that of the reference FEM model.

Figure 5.c compares the sensed signal when we include a parallel DL capacitance-resistance block for the diffuse layer, DL, in series to each HH block before the connection to the resistances of the cleft (i.e., $R_{j,k}^{(in)}$, $R_{j,k}^{(ex)}$ in Figure 3), for different DL resistance values. To emphasize the difference among traces we set μ_{Na}=0.8 and μ_K=1 which gives a large positive signal. As anticipated in the previous section, only when the diffuse layer capacitance outside the membrane is shorted by a small resistance accounting for the transport of ions ($R_{DL1} \leq 1$ nΩ·m^2 (violet curve with squares), consistent with our calculation) the lumped-elements circuit matches the physical FEM model. This effect is not captured if we consider large DL resistances (e.g., $R_{DL3} \geq 1$ kΩ·m^2, (blue curve with triangles up) in parallel to the C_{DL} , as might be erroneously guessed thinking at the steady-state of the membrane when the neuron is at rest with all ionic channels almost closed (i.e., close to zero net trans-membrane ionic flux). This suggests that the most important circuit element is the small R_{DL}; the addition of the C_{DL} would change the circuit behavior only at very high frequencies outside the measurement bandwidth, and therefore can be safely removed from the circuit as a mean to achieve reduced circuit complexity, as will be done in the remaining of this work. Neglecting the R_{DL} and considering the C_{DL} only, instead, (light-blue curve with triangles left) would lead to large errors.

Figure 5.d depicts the signals at the sensing electrode with or without the *upper* HH compartment in the equivalent circuit (values

for *junctional*, *non-junctional* and *upper* areas are given in Table TS2 of the Supplementary Information section). As in Figure 5.c, we consider μ_{Na}=0.8, μ_K=1. The circuit with all the compartments better replicates the FEM response w.r.t. the case without the upper HH, but this last compartment does not play an indispensable role in the qualitative description of the transient responses as the signal deviates by just 14% from the FEM curve for the chosen parameters.

Figure 5.e investigates the effect of the number of HH compartments on the accuracy of the signal waveform. As in Figure 5.c, we consider μ_{Na}=0.8, μ_K=1. For M=8, N=8 the equivalent circuit response is at most 8% off to the FEM one, and converges to it for a larger number of compartments (not shown). Reducing M and N, the waveforms start to deviate from the reference FEM. Nevertheless, they maintain a good match down to simplest case of area contact model of the junction (i.e., M=2) with 4 compartments total. This trend breaks down for the point contact model (i.e., M=1), which misses the averaging effects of the distributed cleft by approximating it with a single-compartment (see also Figure 4.b). Thus, for comparable neuron/electrode sizes, a point contact model overestimates the signals (about a factor of two in this case).

III. Results

Now that the accuracy and robustness of the FEM and equivalent circuit models have been assessed against both experiments and simulations,, we use them in extensive tests to highlight the most important parameters affecting the shape of the recorded signals.

A. Planar Electrode

Figure 6 shows the simulated signals captured by a planar sensing electrode during an action potential. Different parametric studies are presented. In each study, all parameters that are not swept are kept at their default value reported in Tables TS1 and TS2 of the Supplementary Information section. Unless otherwise stated, the equivalent circuit is built following Figure 3 with M=2, N=1 and considering one ion channel depletion conditions to better visualize the curves: μ_{Na}=0.8, μ_K=1.

Figure 6.a reports the V_{sens} waveform for a cleft thickness ranging from 10 to 100 nm, and shows excellent agreement between the FEM and the equivalent circuit models in all cases. For thin clefts [39], the electrode is well sealed by the neuron membrane, and the signal increases due to the large cleft resistance seen by the ionic currents through the cleft. At this nanometric distance the steric effects might be dominant and an electrical double layer description for the cleft/electrode could become inappropriate; however, we verified through an extended *modified*-PNP simulations (see implementation and results in the Supplementary Information) that this is the case only at electrical potentials well beyond the typical extracellular voltage range (i.e., more than tens of mV, see Figures FS1, FS2). For thick clefts, instead, the signal is attenuated due to poor sealing.

Figure 6.b investigates the optimum electrode size for maximum V_{sens} amplitude by sweeping the electrode radius from 2 to 15 µm (while the neuron radius is fixed at 10 µm). In all cases, we keep constant the area where the ion channel density is altered, A_j, to the default value in Table TS1 of the Supplementary Information, regardless of the electrode size. We see that, as discussed in [23], a small electrode collects only a fraction of the extracellular signal activity due to its limited surface area and small sealing resistance. On the other hand, a large electrode (compared to the neuron size) seems even worse, since its uncovered portion, grounded by the electrolyte close to the RE, contributes to reduce the signal coming from the neuron. For the simulated geometry, the optimal electrode

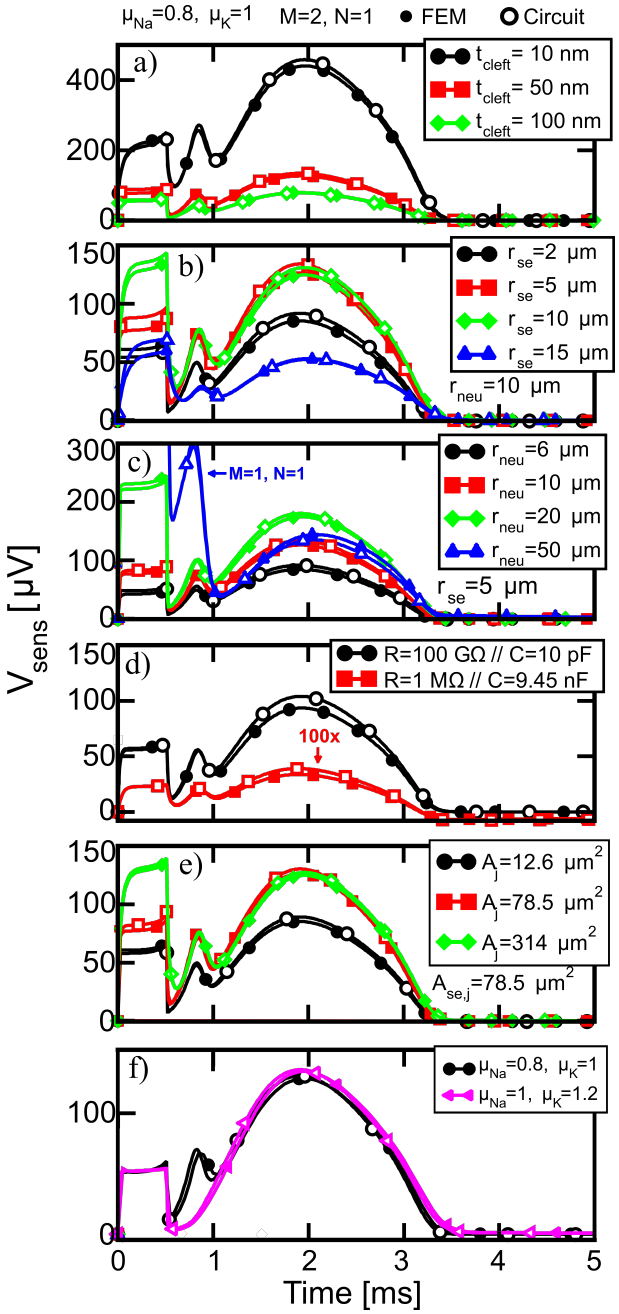

Fig. 6. (a-e) Simulated sensed signal V_{sens} for planar electrodes covered by the neuron as in Figure 2.a or (f) by the ellipsoidal-shaped neuron of Figure 2.b. The panels report the V_{sens} upon sweeping, once at a time: (a) cleft thickness; (b) electrode radius; (c) neuron radius; (d) input impedance of the readout; (e) area where channel density is altered; (f) neuron morphology. Filled symbols=FEM model, open symbols=circuit model, M=2, N=1, μ_{Na}=0.8, μ_K=1 except otherwise stated.

radius is about 0.5-1 times the neuron radius (i.e., r_{se}=5-10 µm) that corresponds to the condition $A_j \leq A_{se,j} \leq \pi r_{neu}^2$.

Figure 6.c examines the impact of different neuron sizes. The morphology remains a dome with constant h_{neu} of 5 µm and r_{neu} ranging from 6 to 50 µm. The smallest neuron delivers the smallest signal to the recording system. The largest positive/negative signals are recorded with 20/50 µm sized neurons. In the latter case, the first observed peak exceeds the scales of the graphs up to approximately 1 mV (not visible). Notice that in the r_{neu}=50 µm case, the circuit has

M=1 (hence it boils down to a point contact model) due to ≈10 times larger dimensions of the neuron compared to the sensing electrode. This result and the one in Figure 5.e give a useful indication of the minimum number of compartments required to build accurate equivalent circuits.

Figure 6.d investigates the effect of the input impedance of the readout focusing on two configurations taken from [38]: i) 100 GΩ resistor in parallel to 10 pF capacitor (i.e., mainly capacitive above ≈0.2 Hz); and ii) 1 MΩ resistor in parallel to 9.45 nF capacitor (i.e., mainly capacitive above ≈17 Hz). These two configurations can be assumed as purely capacitive in the typical AP's spectrum range (≈1-1000 Hz) [5]. Consequently, the sensed extracellular signal, which couples to the readout through the C_{EDLs} at the electrode (see Figure 3), undergoes an almost pure capacitive divider with the readout capacitance. As a result, the sensed waveforms are undistorted and maximized in the small readout capacitance configuration owing to an advantageous capacitive divider. Notice that signals detected with the second configuration (red curves) are magnified 100 times for better visualization.

Figure 6.e reports the sensed voltage by sweeping the extension of the area with altered channel density. The signals are maximized when A_j equals the top surface area of the sensing electrode, that is A_j=$A_{se,j}$=78.5 μm^2 in this case. Beyond this condition, we do not find any improvements, even if we alter the channel density in the whole bottom membrane (A_j=314 μm^2).

Figure 6.f shows the V_{sens} for the ellipsoidal neuron in Figure 2.b. This alternative neuron morphology is useful to analyze the effect of non-constant cleft thickness on the ability of our approach to build accurate equivalent circuits that replicate the FEM response even in complex geometries. We used a piece-wise constant thickness approximation for the clefts whose thickness increases as we approach the edge of the neuron. In this case, we set N=1; thus, we have a constant thickness for the non-junctional lateral compartment. Figure 6.f shows the recorded signal for all μ_{X_i} combinations. Also in this case the extracted equivalent circuit matches well the FEM results despite the simplification of curved clefts as boxes with constant thicknesses.

B. Mushroom Electrode

Mushroom electrodes (Figure 2.c) are a promising category of extracellular protruding electrodes for neural sensing [4], [5], [39]. We report in this section a few parametric studies of this electrode morphology.

Figure 8 shows the responses of the FEM and equivalent circuit models for the structure sketched in Figure 2.c, where the cap of the mushroom is engulfed by the neuron. Figure 7 shows how the engulfment condition converts the planar cleft above a planar electrode into an equivalent (i.e., with the same area) hemi-ellipsoid junctional cleft, that is the one in between the neuron and the mushroom cap. This curvature bends the current density streamlines from the center of the mushroom cap to its edge and might affect the signal sensed by the electrode. As a matter of fact, Figure 8.a shows the response if one approximates the cleft at the mushroom's cap as a planar disk (dashed lines) rather than a curved one (solid lines). This approximation, indeed, is inconsistent with the FEM.

To consider the curvature of the cleft when computing the resistances in the junctional blocks we followed the formula in [62] for concentric rings with a constant cleft at the mushroom's cap. In analogy with steps 1-3 of Figure 3, we define an *equivalent* planar representation of the junctional cleft surface and split it into M rings having constant radius pitch, see Figure 7. Accordingly, the hemi-ellipsoidal cleft is then partitioned into M rings having the same areas of the rings defined in the equivalent planar representation. Each *k-th* ring subtends a *k-th* angle in the mushroom, which thus divides

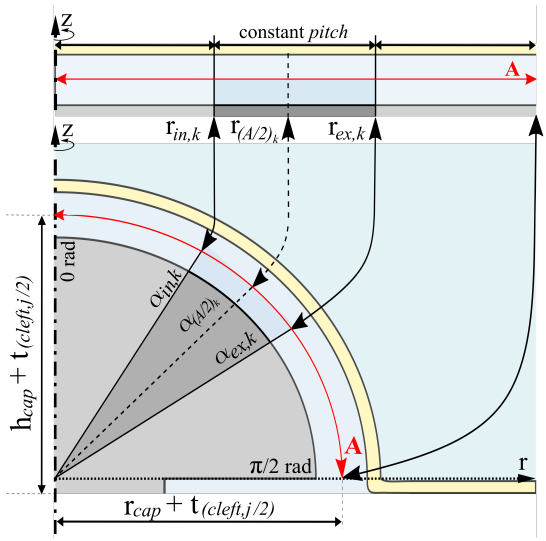

Fig. 7. Sketch of (top) a planar cleft above a planar electrode equivalent to (bottom) the hemi-ellipsoidal cleft above the mushroom-shaped electrode. The area of the planar cleft A is the same as the top surface of the mid-height hemi-ellipsoid cleft and both are split in rings of constant *pitch*. The angles $\alpha_{in,k}$, $\alpha_{(A/2)_k}$, and $\alpha_{ex,k}$ in the mushroom-shaped cleft can be computed from the corresponding radii $r_{in,k}$, $r_{(A/2)_k}$, and $r_{ex,k}$ according to (20).

the π/2 rad angle into M portions. In this equivalent planar mapping procedure, the hemi-ellipsoid is regarded as a hemi-sphere; thus, a generic angle α w.r.t. the vertical direction (z-axis) can be computed from the corresponding radius r on the planar disk according to

$$\alpha \simeq \frac{r}{\sqrt{\frac{\left(r_{cap}+t_{(cleft,j/2)}\right)^2+\left(h_{cap}+t_{(cleft,j/2)}\right)^2}{2}}}. \qquad (20)$$

Exploiting again the analogies with the planar electrode in Figure 3, every *k-th* sub-angle comprises an internal angle contribution from $\alpha_{in,k}$ to $\alpha_{(A/2)_k}$, and an external one from $\alpha_{(A/2)_k}$ to $\alpha_{ex,k}$. Doing so, the *k-th* internal and external junctional sealing resistances for curved clefts can be computed as [62]:

$$R_{j,k}^{(in)} = \frac{1}{2\pi\sigma_{el}t_{cleft,j}} \ln\left(\frac{\mathrm{tg}\left(0.5\,\alpha_{(A/2)_k}\right)}{\mathrm{tg}(0.5\,\alpha_{in,k})}\right)$$
$$R_{j,k}^{(ex)} = \frac{1}{2\pi\sigma_{el}t_{cleft,j}} \ln\left(\frac{\mathrm{tg}(0.5\,\alpha_{ex,k})}{\mathrm{tg}\left(0.5\,\alpha_{(A/2)_k}\right)}\right) \qquad (21)$$

where $\mathrm{tg}(\cdot)$ is the tangent function, $\alpha_{(A/2)_k}$ is the angle at which the area of *k-th* compartment divides into two, k={1,...,M}, $\alpha_{in,1} = 0$ rad, and $\alpha_{ex,M} = \pi/2$ rad.

The transient response of the equivalent circuit varying the cleft thickness and the electrode size is reported in Figure 8.b and 8.c, respectively. Both plots show an excellent agreement between the FEM results and the equivalent circuit description, demonstrating once more the robustness of the proposed partitioning of the junctional neuron/electrode area, for the determination of accurate lumped-element model parameters.

In Figure 8.b we see that the effect of the cleft is similar for the mushroom and planar electrodes (see Figure 6.a) for the same reasons discussed in the previous section.

Figure 8.c analyzes the effect of the mushroom size. The cap radius spans from 1 to 4 μm for constant r_{neu}=10 nm. In all cases, the neuron fully engulfs the cap at a constant cleft regardless of the electrode

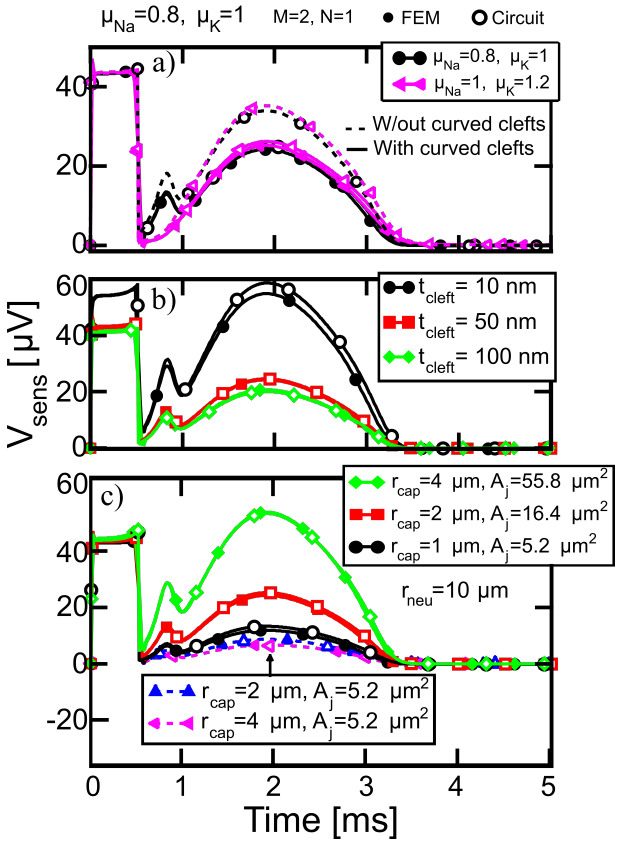

Fig. 8. Simulated sensed signal V_{sens} for mushroom electrodes as in Figure 2.c using the FEM setup (filled symbols) and the corresponding equivalent circuit (open symbols): (a) by approximating the mushroom's cleft as planar (dashed) and curved (solid), and considering the curvature of the cleft in the circuit for different values (b) of cleft thickness and (c) of mushroom dimensions. Filled symbols=FEM model, open symbols=circuit model, M=2, N=1, μ_{Na}=0.8, μ_K=1 except otherwise stated.

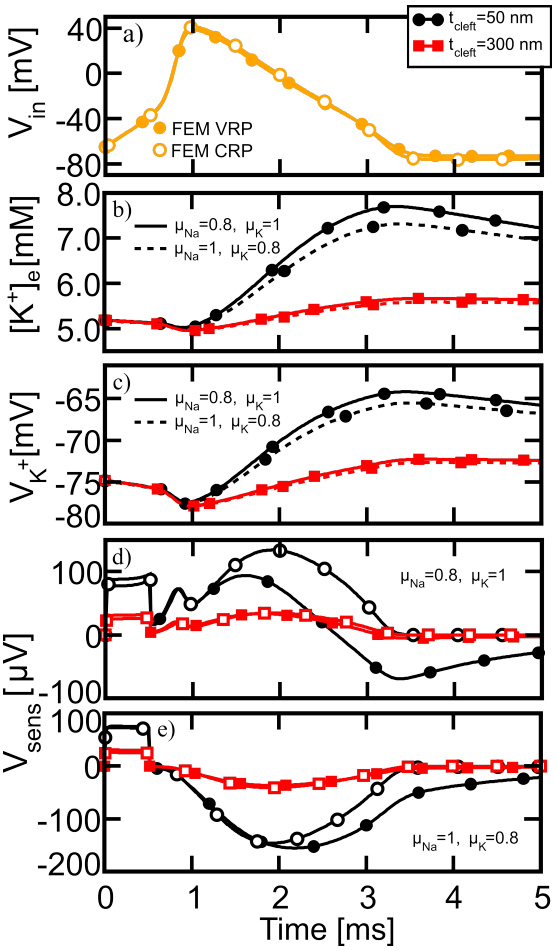

Fig. 9. (a) Intracellular potential, (b) potassium ion concentration in the proximity of the bottom membrane, (c) corresponding potassium reversal potential, and (d-e) potential sensed AP transient response signals for the recording system in Figure 2.a. FEM simulations are performed with variable reversal potentials, i.e., (5) active (filled symbols) or constant reversal potentials (open symbols) for cleft thicknesses of 50 nm and 300 nm. The density of ion channels is: (b,c,d) μ_{Na}=0.8, μ_K=1 and (b,c,e) μ_{Na}=1, μ_K=0.8. CRP=constant reversal potentials, VRP=variable reversal potentials.

size; thus, the engulfed surface area corresponds approximately to the external surface of the cap, denoted as $A_{se,j}$. In this test, we consider that the junctional area with altered channel density: i) changes according to the actual engulfed area, i.e., A_j=$A_{se,j}$ (solid lines); or ii) is constant at A_j=5.2 μm^2 (dashed lines). The results suggest that a large mushroom electrode collects a larger useful signal than smaller ones only if the aggregation/depletion of channels spreads throughout the entire engulfed membrane portion. On the other hand, if the area where the channel density is altered remains constant, the signal is maximized as long as $A_{se,j} \leq A_j$. Similar behavior has been observed also for the planar electrode in Figure 6.b.

C. Effect of ion diffusion on the reversal potentials

In this last analysis, we compute by the FEM, and self-consistently update at each time-step, the reversal potentials of the ions according to the actual ionic concentrations at the HH membrane ((5) in Figure 1). We compare these new FEM simulations with variable reversal potentials (VRP) to the ones with the constant reversal potentials (CRP) in Table TS1 for the device structure in Figure 2.a. Furthermore, we investigate how the cleft resistivity and geometry affect the reversal potentials during an AP spike.

Figure 9 compares the VRP and CRP responses for t_{cleft}=50 nm and 300 nm, and for μ_{Na}=0.8, μ_K=1 or μ_{Na}=1, μ_K=0.8. In particular, Figure 9.a shows that the intracellular potential waveforms are essentially the same in both cases.

Figure 9.b shows the waveform of the potassium concentration $[K^+]_e$ (*e* for extracellular) on the vertical symmetry axis at the extracellular side of the bottom membrane. The intracellular $[K^+]$ is almost constant (not shown). Results for μ_{Na}=0.8, μ_K=1 and μ_{Na}=1, μ_K=0.8 exhibit very similar features. The ions' confinement for t_{cleft}=50 nm causes a larger increase of $[K^+]_e$ compared to the t_{cleft}=300 nm case, as expected. The relative increase of $[Cl^-]_e$ and $[Na^+]_e$ (not shown) are less pronounced compared to one of $[K^+]_e$ and non-influential for the following discussion.

Figure 9.c shows the time-varying potassium reversal potential obtained with (5) and K^+ concentration from panel .b. For 50 nm thick cleft, the V_{K^+} remarkably deviates from the rest value (≈ -77 mV [33]), which is not the case for the 300 nm thick cleft. The change in $[K^+]_e$ affects the signal waveform in panels d-e. The $[Cl^-]$ and $[Na^+]$ reversal potentials computed with (5) at the bottom membrane (not shown) remain almost constant at their baseline value (see Table TS1 in the Supplementary Information).

Figure 9.d and Figure 9.e depict the sensed signal for μ_{Na}=0.8, μ_K=1 and μ_{Na}=1, μ_K=0.8, respectively. The difference between VRP and CRP models is small for $t_{cleft} \geq$100 nm, and definitely negligible for $t_{cleft} \geq$300 nm. For a thin cleft of 50 nm instead the VRP signals

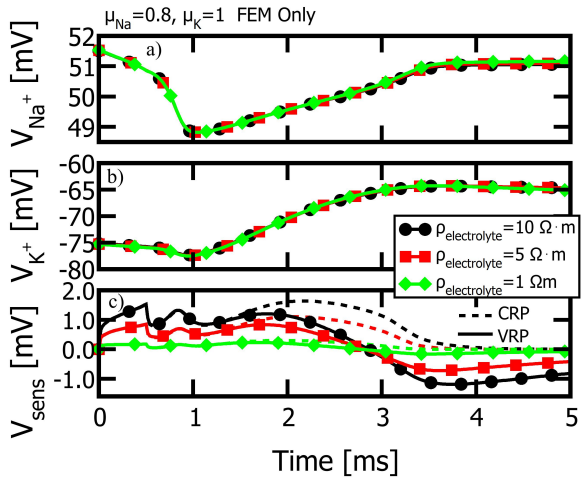

Fig. 10. (a) Na^+, (b) K^+ reversal potentials and (c) sensed signal waveforms during an AP for a few values of electrolyte resistivity for the planar electrode in Figure 2.a and default dimensions in Table TS2 of the Supplementary Information. CRP sensed signals (dashed curves) are reported for comparison. Reversal potentials are sampled at the bottom side of the neuron membrane in the center of the structure. μ_{Na}=0.8, μ_K=1, t_{cleft}=50 nm.

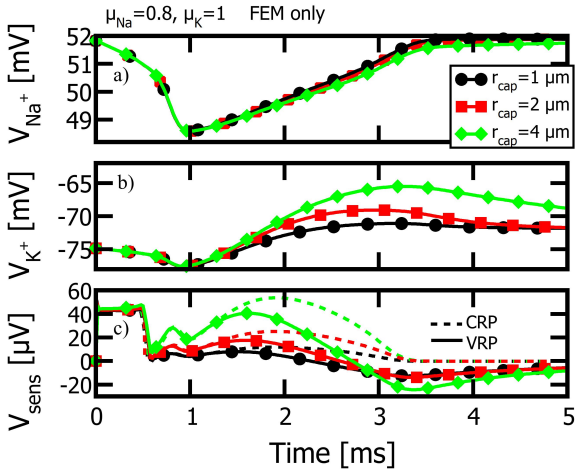

Fig. 11. Same as in Figure 10 but for a few values of cap radius for the mushroom electrode in Figure 2.c and default dimensions in Table TS2 of the Supplementary Information. μ_{Na}=0.8, μ_K=1, t_{cleft}=50 nm.

significantly depart from the CRP case. This change is due to K^+ accumulation in the cleft and the consequent change of V_{K^+} w.r.t. the baseline value.

The equivalent circuit results closely match the FEM with *constant* reversal potential (CRP), as expected. The FEM with *variable* reversal potentials (VRP), instead, shows new features not captured by equivalent circuit models.

Figure 10 and Figure 11 elucidate how the cleft resistivity and geometry drive the reversal potentials to depart from the baseline value. While the Na^+ reversal potentials do not change much compared to the baseline value (Figure 10.a and Figure 11.a), V_{K^+} exhibits a significant modulation.

Figure 10.b shows that electrolyte resistivity does not change the V_{K^+} in the time-scale of an action potential. This might suggest the deviations of the VRP signals (solid curves) from the CRP ones (dashed curves) in Figure 10.c depend mainly on the increased neuron/electrode sealing resistance, and not on the accumulation of K^+ in the tiny cleft in the time-scale of an AP.

Figure 11.b shows that the largest deviation of the K^+ reversal potential occurs for the largest cap radius, i.e., larger extension and smaller curvature of the neuron/cap cleft. This suggests that the length of the clefts is more effective than the curvature in increasing the cleft's K^+ concentration (not shown) and consequently the V_{K^+}. This dynamic reflects on the sensed waveforms (Figure 11.c) showing larger deviations for longer clefts (i.e., larger r_{cap}) compared to the corresponding CRP traces.

We also studied the effect of steric volume exclusion on the reversal potentials (see Figure FS2 in the Supplementary Information), but we found them negligible even in ultra-thin clefts (e.g., 10 nm).

This extensive analysis suggests that the self-consistent update of the reversal potential is important when the cleft is thinner than 100 nm. However, one should consider that Figure 9 represents a kind of worst-case scenario, since the model does not include homeostatic mechanisms at the neural membrane (e.g., the Na^+-K^+-pumps) nor the astrocytes surrounding the neuron that could buffer the extracellular potassium concentration. Furthermore, we assumed that changes of $[K^+]_e$ instantaneously translate into changes of the reversal potential, both points requiring further investigation in the future.

IV. Discussion

We have developed a FEM simulation framework that may serve as a basis for the analysis, identification, and optimization of extracellular recording electrodes. The model self-consistently couples ionic transport, action potential generation, reversal potential update, and extracellular signal sensing. We validated this complex simulation framework by assessing its ability to reproduce published experimental and simulated extracellular signals.

The validated FEM framework was then used to advance the state-of-the-art of area contact (ACM) models by developing a robust and structured approach to construct multi-compartment equivalent circuit models for the neuron/electrode system. Special care has been paid to correctly partition the system, and to model the interaction between the HH blocks representing the neuron membrane and the cleft resistance. We highlight that the examined physical system has axial symmetry, a common approximation in this field. Hence, FEM simulations are solved in cylindrical coordinates to reduce the computational effort. This approximation allowed us to adopt analytical formulas for the lumped elements in the equivalent circuit, only based on the system's radial and vertical dimensions.

Guidelines have been presented to determine the minimum number of compartments for neurons and electrodes of different shapes (dome/elliptical, and planar/mushroom, respectively). ACM circuits generated along these guidelines have been proven to accurately capture the distributed effects at the neuron/electrode clefts put in evidence by the FEM, whereas traditional point contact circuit models overestimate the signal amplitudes.

We also verified that steric volume exclusion is negligible in thin clefts down to 10 nm even in the presence of a significant amount of extra particles/molecules limiting ion transport. This is essentially due to the small value of the extracellular voltages.

To ease the use and circulation of our results, we provide the link to the external GitHub repository "Leva-et-al-lumped-element-equivalent-circuit" containing examples of lumped-element equivalent circuit schematics for transient analysis based on the open-source freely-distributed LTSpice simulation software.

V. Conclusions

A systematic analysis led us to derive or confirm design guidelines to maximize the quality of the sensed signal. The main findings are:

1) the electrolyte cleft should be as thin as possible for large signal amplitude but below approximately 100 nm variations of the reversal potentials may occur;
2) the size of the electrode should be comparable to the size of the portion of the neuron where the density of ion channels is altered but should not exceed the neuron size;
3) in the absence of a protein layer between the neuron and the contact (that has been assumed in [32], [37] but not considered in the present work), the diffuse-layer capacitance at the membrane should be removed from the equivalent circuit, unless a small diffuse-layer resistance is placed in parallel;
4) ACMs with M$\geq$2 yield a more accurate equivalent circuit description of the junction when neuron and electrode have comparable size; PCMs (M=1) can be used for neurons much larger than the electrode.

The developed methodology to build lumped-element circuits allows to derive representations of neuron/electrode interfaces with few circuit elements without losing accuracy compared to the more complex and physics-based FEM. The circuit, however, does not account for the interplay between extracellular concentrations and reversal potential changes. To the best of our knowledge, this is a unique feature of the proposed FEM model.

As a final remark, we point out that the developed FEM model is based on a general-purpose simulation framework and solver. Hence, it is upward scalable and amenable to include more complex descriptions of the neuron morphology and physiology, and more complete models of the readout circuit.

ACKNOWLEDGMENT

The authors thank Julian Leandro Mele for the many fruitful discussions and for the suggestions in setting up the FEM simulation framework.

REFERENCES

[1] A. Tanwar, H. A. Gandhi, D. Kushwaha, and J. Bhattacharya, "A review on microelectrode array fabrication techniques and their applications," *Materials Today Chemistry*, vol. 26, 12 2022. 10.1016/j.mtchem.2022.101153.

[2] C. A. Thomas, P. A. Springer, G. E. Loeb, Y. Berwald-Netter, and L. M. Okun, "A miniature microelectrode array to monitor the bioelectric activity of cultured cells," *Experimental Cell Research*, vol. 74, pp. 61–66, 9 1972. 10.1016/0014-4827(72)90481-8.

[3] J. Pine, "Recording action potentials from cultured neurons with extracellular microcircuit electrodes," *Journal of Neuroscience Methods*, vol. 2, pp. 19–31, 2 1980. 10.1016/0165-0270(80)90042-4.

[4] F. Leva, P. Palestri, , and L. Selmi, "Multiscale simulation analysis of passive and active micro/nano-electrodes for CMOS-based in-vitro neural sensing devices," *Philosophical Transactions of the Royal Society A: Mathematical, Physical and Engineering Sciences*, 2021. 10.1098/rsta.2021.0013.

[5] M. E. Spira and A. Hai, "Multi-electrode array technologies for neuroscience and cardiology," *Nature nanotechnology*, vol. 8, no. 2, pp. 83–94, 2013. 10.1038/nnano.2012.265.

[6] G. Zeck, F. Jetter, L. Channappa, G. Bertotti, and R. Thewes, "Electrical Imaging: Investigating Cellular Function at High Resolution," 11 2017. 10.1002/adbi.201700107.

[7] D. Tsai, D. Sawyer, A. Bradd, R. Yuste, and K. L. Shepard, "A very large-scale microelectrode array for cellular-resolution electrophysiology," *Nature Communications*, vol. 8, 12 2017. 10.1038/s41467-017-02009-x.

[8] R. Plosney and C. R. Barr, *Bioelectricity A Quantitative Approach*. Springer, 3rd ed. ed., 2007.

[9] C. Koch and I. Segev, *Methods in Neuronal Modeling: from Ions to Networks*. MIT Press, 2nd ed. ed., 1998.

[10] H. Lindén, E. Hagen, S. Łeski, E. S. Norheim, K. H. Pettersen, and G. T. Einevoll, "LFPy: A tool for biophysical simulation of extracellular potentials generated by detailed model neurons," *Frontiers in Neuroinformatics*, vol. 7, no. JAN, 2014. 10.3389/fninf.2013.00041.

[11] G. R. Holt and C. Koch, "Electrical interactions via the extracellular potential near cell bodies," *Journal of Computational Neuroscience*, vol. 6, no. 2, 1999. 10.1023/A:1008832702585.

[12] C. H. Lubba, Y. Le Guen, S. Jarvis, N. S. Jones, S. C. Cork, A. Eftekhar, and S. R. Schultz, "PyPNS: Multiscale Simulation of a Peripheral Nerve in Python," *Neuroinformatics*, vol. 17, no. 1, 2019. 10.1007/s12021-018-9383-z.

[13] T. V. Ness, C. Chintaluri, J. Potworowski, S. Łęski, H. Głąbska, D. K. Wójcik, and G. T. Einevoll, "Modelling and Analysis of Electrical Potentials Recorded in Microelectrode Arrays (MEAs)," *Neuroinformatics*, vol. 13, no. 4, 2015. 10.1007/s12021-015-9265-6.

[14] R. Bestel, U. Van Rienen, C. Thielemann, and R. Appali, "Influence of Neuronal Morphology on the Shape of Extracellular Recordings with Microelectrode Arrays: A Finite Element Analysis," *IEEE Transactions on Biomedical Engineering*, vol. 68, no. 4, 2021. 10.1109/TBME.2020.3026635.

[15] A. Agudelo-Toro and A. Neef, "Computationally efficient simulation of electrical activity at cell membranes interacting with self-generated and externally imposed electric fields," *Journal of Neural Engineering*, vol. 10, no. 2, 2013. 10.1088/1741-2560/10/2/026019.

[16] C. Moulin, A. Glière, D. Barbier, S. Joucla, B. Yvert, P. Mailley, and R. Guillemaud, "A new 3-D finite-element model based on thin-film approximation for microelectrode array recording of extracellular action potential," *IEEE Transactions on Biomedical Engineering*, vol. 55, no. 2, 2008. 10.1109/TBME.2007.903522.

[17] A. Solbrå, A. W. Bergersen, J. van den Brink, A. Malthe-Sørenssen, G. T. Einevoll, and G. Halnes, "A Kirchhoff-Nernst-Planck framework for modeling large scale extracellular electrodiffusion surrounding morphologically detailed neurons," *PLoS Computational Biology*, vol. 14, no. 10, 2018. 10.1371/journal.pcbi.1006510.

[18] A. J. Ellingsrud, A. Solbrå, G. T. Einevoll, G. Halnes, and M. E. Rognes, "Finite Element Simulation of Ionic Electrodiffusion in Cellular Geometries," *Frontiers in Neuroinformatics*, vol. 14, 2020. 10.3389/fninf.2020.00011.

[19] J. Pods, J. Schönke, and P. Bastian, "Electrodiffusion models of neurons and extracellular space using the poisson-nernst-planck equations - Numerical simulation of the intra- and extracellular potential for an axon model," *Biophysical Journal*, vol. 105, no. 1, 2013. 10.1016/j.bpj.2013.05.041.

[20] J. Pods, "A comparison of computational models for the extracellular potential of neurons," *Journal of Integrative Neuroscience*, vol. 16, no. 1, 2017. 10.3233/JIN-170009.

[21] P. Fromherz, "Neuroelectronic interfacing: semiconductor chips with ion channels, nerve cells, and brain," in *Nanoelectronics and Information Technology* (R. Waser, ed.), ch. 32, pp. 781–810, Berlin: Wiley-VCH, 2003.

[22] M. Pabst, G. Wrobel, S. Ingebrandt, F. Sommerhage, and A. Offenhäusser, "Solution of the Poisson-Nernst-Planck equations in the cell-substrate interface," *European Physical Journal E*, vol. 24, no. 1, 2007. 10.1140/epje/i2007-10204-6.

[23] F. Leva, C. Verardo, P. Palestri, and L. Selmi, "Multiphysics finite-element modeling of the neuron/electrode electrodiffusive interaction," in *2022 IEEE Sensors*, IEEE, 2022. 10.1109/SENSORS52175.2022.9967049.

[24] P. Fromherz, A. Offenhäusser, T. Vetter, and J. Weis, "A neuron-silicon junction: A retzius cell of the leech on an insulated-gate field-effect transistor," *Science*, vol. 252, no. 5010, pp. 1290–1293, 1991. 10.1126/science.1925540.

[25] M. Grattarola and S. Martinoia, "Modeling the neuron-microtransducer junction: from extracellular to patch recording," *IEEE Transactions on Biomedical Engineering*, vol. 40, no. 1, pp. 35–41, 1993. 10.1109/10.204769.

[26] L. Chua, "Device modeling via nonlinear circuit elements," *IEEE Transactions on Circuits and Systems*, vol. 27, no. 11, pp. 1014–1044, 1980. 10.1088/0957-4484/23/6/065202.

[27] M. Parodi and M. Storace, "On a circuit representation of the hodgkin and huxley nerve axon membrane equations," *International journal of circuit theory and applications*, vol. 25, no. 2, pp. 115–124, 1997. 10.1002/(SICI)1097-007X(199703/04)25:2¡115::AID-CTA957¿3.0.CO;2-#.

[28] D. Biolek, V. Biolkova, and Z. Kolka, "Spice models of memristive devices forming a model of hodgkin-huxley axon," in *2013 18th Inter-*

national Conference on Digital Signal Processing (DSP), pp. 1–5, IEEE, 2013. 10.1109/ICDSP.2013.6622743.

[29] R. Schätzthauer and P. Fromherz, "Neuron–silicon junction with voltage-gated ionic currents," *European Journal of Neuroscience*, vol. 10, no. 6, pp. 1956–1962, 1998. 10.1046/j.1460-9568.1998.00205.x.

[30] S. Martinoia, P. Massobrio, M. Bove, and G. Massobrio, "Cultured neurons coupled to microelectrode arrays: circuit models, simulations and experimental data," *IEEE Transaction on Biomedical Engineering*, vol. 51, no. 5, pp. 859–863, 2004. 10.1109/TBME.2004.826607.

[31] A. Hai, J. Shappir, and M. E. Spira, "Long-term, multisite, parallel, in-cell recording and stimulation by an array of extracellular microelectrodes," *Journal of Neurophysiology*, vol. 104, no. 1, pp. 559–568, 2010. 10.1152/jn.00265.2010.

[32] V. Thakore, P. Molnar, and J. J. Hickman, "An optimization-based study of equivalent circuit models for representing recordings at the neuron–electrode interface," *IEEE Transactions on Biomedical Engineering*, vol. 59, no. 8, pp. 2338–2347, 2012. 10.1109/TBME.2012.2203820.

[33] A. L. Hodgkin and A. F. Huxley, "A quantitative description of membrane current and its application to conduction and excitation in nerve," *The Journal of Physiology*, vol. 117, no. 4, pp. 500–544, 1952. 10.1113/jphysiol.1952.sp004764.

[34] P. Fromherz, "Extracellular recording with transistors and the distribution of ionic conductances in a cell membrane," *European biophysics journal: EBJ*, vol. 28, no. 3, p. 254, 1999. 10.1007/s002490050206.

[35] M. Brittinger and P. Fromherz, "Field-effect transistor with recombinant potassium channels: Fast and slow response by electrical and chemical interactions," *Applied Physics A: Materials Science and Processing*, vol. 81, no. 3, 2005. 10.1007/s00339-005-3272-7.

[36] P. Massobrio, G. Massobrio, and S. Martinoia, "Interfacing cultured neurons to microtransducers arrays: A review of the neuro-electronic junction models," *Frontiers in Neuroscience*, vol. 10, no. JUN, 2016. 10.3389/fnins.2016.00282.

[37] G. Massobrio, S. Martinoia, and P. Massobrio, "Equivalent circuit of the neuro-electronic junction for signal recordings from planar and engulfed micro-nano-electrodes," *IEEE Transactions on Biomedical Circuits and Systems*, vol. 12, no. 1, pp. 3–12, 2018. 10.1109/TBCAS.2017.2749451.

[38] L. Guo, "Perspectives on electrical neural recording: a revisit to the fundamental concepts," *Journal of Neural Engineering*, vol. 17, p. 013001, feb 2020. 10.1088/1741-2552/ab702f.

[39] S. M. Ojovan, N. Rabieh, N. Shmoel, H. Erez, E. Maydan, A. Cohen, and M. E. Spira, "A feasibility study of multi-site, intracellular recordings from mammalian neurons by extracellular gold mushroom-shaped microelectrodes," *Scientific reports*, vol. 5, no. 1, pp. 1–14, 2015. 10.1038/srep14100.

[40] M. Bove, G. Massobrio, S. Martinoia, and M. Grattarola, "Realistic simulations of neurons by means of an ad hoc modified version of spice," *Biological cybernetics*, vol. 71, no. 2, pp. 137–145, 1994. 10.1007/BF00197316.

[41] N. Joye, A. Schmid, and Y. Leblebici, "Electrical modeling of the cell-electrode interface for recording neural activity from high-density microelectrode arrays," *Neurocomputing*, vol. 73, 2009. 10.1016/j.neucom.2009.09.006.

[42] M. Schottdorf, B. Hofmann, E. Kätelhön, A. Offenhäusser, and B. Wolfrum, "Frequency-dependent signal transfer at the interface between electrogenic cells and nanocavity electrodes," *Physical Review E - Statistical, Nonlinear, and Soft Matter Physics*, vol. 85, 3 2012. 10.1103/PhysRevE.85.031917.

[43] Comsol, Inc., Comsol Multiphysics v. 6.0.

[44] A. J. Bard and L. R. Faulkner, *Electrochemical methods: fundamentals and applications*. John Wiley & Sons, Inc., 2nd ed. ed., 2001.

[45] R. Jolivet, J. S. Coggan, I. Allaman, and P. J. Magistretti, "Multi-timescale Modeling of Activity-Dependent Metabolic Coupling in the Neuron-Glia-Vasculature Ensemble," *PLoS Computational Biology*, vol. 11, no. 2, 2015. 10.1371/journal.pcbi.1004036.

[46] E. Hay, S. Hill, F. Schürmann, H. Markram, and I. Segev, "Models of neocortical layer 5b pyramidal cells capturing a wide range of dendritic and perisomatic active properties," *PLoS Computational Biology*, vol. 7, no. 7, 2011. 10.1371/journal.pcbi.1002107.

[47] K. J. Angelides, L. W. Elmer, D. Loftus, and E. Elson, "Distribution and lateral mobility of voltage-dependent sodium channels in neurons.," *Journal of Cell Biology*, vol. 106, pp. 1911–1925, 06 1988. 10.1083/jcb.106.6.1911.

[48] A. Cohen, J. Shappir, S. Yitzchaik, and M. E. Spira, "Experimental and theoretical analysis of neuron-transistor hybrid electrical coupling: The relationships between the electro-anatomy of cultured Aplysia neurons and the recorded field potentials," *Biosensors and Bioelectronics*, vol. 22, pp. 656–663, 12 2006. 10.1016/j.bios.2006.02.005.

[49] S. Vassanelli and P. Fromherz, "Transistor probes local potassium conductances in the adhesion region of cultured rat hippocampal neurons," *Journal of Neuroscience*, vol. 19, no. 16, 1999. 10.1523/jneurosci.19-16-06767.1999.

[50] J. Buitenweg, W. Rutten, and E. Marani, "Modeled channel distributions explain extracellular recordings from cultured neurons sealed to microelectrodes," *IEEE Transactions on Biomedical Engineering*, vol. 49, no. 12, pp. 1580–1590, 2002. 10.1109/TBME.2002.805555.

[51] B. Straub, E. Meyer, and P. Fromherz, "Recombinant maxi-K channels on transistor, a prototype of iono-electronic interfacing," *Nature Biotechnology*, vol. 19, no. 2, 2001. 10.1038/84369.

[52] M. Schottdorf, B. Hofmann, E. Kätelhön, A. Offenhäusser, and B. Wolfrum, "Frequency-dependent signal transfer at the interface between electrogenic cells and nanocavity electrodes," *Physical Review E - Statistical, Nonlinear, and Soft Matter Physics*, vol. 85, no. 3, 2012. 10.1103/PhysRevE.85.031917.

[53] A. Marcantoni, G. Chiantia, G. Tomagra, E. Hidisoglu, C. Franchino, V. Carabelli, and E. Carbone, "Two firing modes and well-resolved Na+, K+, and Ca2+ currents at the cell-microelectrode junction of spontaneously active rat chromaffin cell on MEAs," *Pflugers Archiv European Journal of Physiology*, pp. 1–22, oct 2022. 10.1007/S00424-022-02761-0.

[54] A. Blau, "Cell adhesion promotion strategies for signal transduction enhancement in microelectrode array in vitro electrophysiology: An introductory overview and critical discussion," *Current Opinion in Colloid and Interface Science*, vol. 18, no. 5, 2013. 10.1016/j.cocis.2013.07.005.

[55] D. Robinson, "The electrical properties of metal microelectrodes," *Proceedings of the IEEE*, vol. 56, no. 6, pp. 1065–1071, 1968. 10.1109/PROC.1968.6458.

[56] V. Viswam, M. E. J. Obien, F. Franke, U. Frey, and A. Hierlemann, "Optimal electrode size for multi-scale extracellular-potential recording from neuronal assemblies," *Frontiers in Neuroscience*, vol. 13, 2019. 10.3389/fnins.2019.00385.

[57] M. Voelker and P. Fromherz, "Signal transmission from individual mammalian nerve cell to field-effect transistor," *Small*, vol. 1, no. 2, pp. 206–210, 2004. 10.1002/smll.200400077.

[58] M. Pospischil, M. Toledo-Rodriguez, C. Monier, Z. Piwkowska, T. Bal, Y. Frégnac, H. Markram, and A. Destexhe, "Minimal hodgkin–huxley type models for different classes of cortical and thalamic neurons," *Biological cybernetics*, vol. 99, pp. 427–441, 2008. 10.1007/s00422-008-0263-8.

[59] F. Leva, P. Palestri, and L. Selmi, "A simulation study of fet-based nanoelectrodes for active intracellular neural recordings," in *2022 22nd IEEE International Conference on Nanotechnology (IEEE-NANO 2022)*, IEEE, 2022. 10.1109/NANO54668.2022.9928642.

[60] A. L. Hodgkin and A. F. Huxley, "A quantitative description of membrane current and its application to conduction and excitation in nerve," *The Journal of physiology*, vol. 117, no. 4, p. 500, 1952. 10.1113/jphysiol.1952.sp004764.

[61] J. F. Fohlmeister, E. D. Cohen, and E. A. Newman, "Mechanisms and distribution of ion channels in retinal ganglion cells: Using temperature as an independent variable," *Journal of Neurophysiology*, vol. 103, no. 3, pp. 1357–1374, 2010. PMID: 20053849.

[62] A. Fendyur, N. Mazurski, J. Shappir, and M. Spira, "Formation of essential ultrastructural interface between cultured hippocampal cells and gold mushroom-shaped mea- toward "in-cell" recordings from vertebrate neurons," *Frontiers in Neuroengineering*, vol. 4, 2011. 10.3389/fneng.2011.00014.